[^{18}F]DPA-714 PET Imaging Reveals Global Neuroinflammation in Zika Virus-Infected Mice

Kyle Kuszpit[1†], Bradley S. Hollidge[2†], Xiankun Zeng[3], Robert G. Stafford[1], Sharon Daye[3], Xiang Zhang[4], Falguni Basuli[4], Joseph W. Golden[2], Rolf E. Swenson[4], Darci R. Smith[2†*], Thomas M. Bocan[1†*]

Running Head: PET Imaging of Zika Virus-Induced Neuroinflammation

Manuscript Category: Article

Affiliations:

[1]Molecular and Translational Sciences Division, [2]Virology Division, [3]Pathology Division, U.S. Army Medical Research Institute of Infectious Diseases, 1425 Porter St., Ft. Detrick, MD., 21702 USA

[4]Imaging Probe Development Center, National Heart, Lung, and Blood Institute, National Institutes of Health, 9800 Medical Center Drive, Bldg. B., #2034
Bethesda, MD., 20892 USA

†These authors contributed equally to this work.

*Corresponding authors: Thomas Bocan; thomas.m.bocan.ctr@mail.mil; (301) 619-2647 and Darci Smith; darci.r.smith.ctr@mail.mil; (301) 619-4125

Abstract:

Purpose: The association of Zika virus (ZIKV) infection and the development of neurological sequelae require a better understanding of the pathogenic mechanisms causing severe disease. The purpose of this study was to evaluate the ability and sensitivity of positron emission tomography (PET) imaging using [^{18}F]DPA-714, a translocator protein (TSPO) 18 kDa radioligand, to detect and quantify neuroinflammation in ZIKV-infected mice.

Procedures: We assessed ZIKV-induced pathogenesis in wild-type C57BL/6 mice treated with an antibody to disrupt type I interferon (IFN) signaling. [^{18}F]DPA-714 PET imaging was performed on days 3, 6, and 10 post-infection (PI), and tissues were subsequently processed for histological evaluation, quantification of microgliosis, and detection of viral RNA by *in situ* hybridization (ISH).

Results: In susceptible ZIKV-infected mice, viral titers in the brain increased from day 3 to day 10 PI. Over this span, these mice showed a 2- to 6-fold increase in global brain neuroinflammation using [^{18}F]DPA-714 PET imaging despite limited, regional detection of viral RNA. No measurable increase in ionized calcium binding adaptor molecule 1 (Iba-1) expression was noted at day 3 PI; however, there was a modest increase at day 6 PI and a significant ~4-fold increase in Iba-1 expression at day 10 PI in the susceptible ZIKV-infected group relative to controls.

Conclusions: The results of the current study demonstrate that global neuroinflammation plays a significant role in the progression of ZIKV infection and that [^{18}F]DPA-714 PET imaging is a sensitive tool relative to histology for the detection of neuroinflammation. [^{18}F]DPA-714 PET imaging and potentially other PET probes may be useful in

dynamically characterizing the pathology associated with neurotropic viruses and the evaluation of therapeutics being developed for treatment of infectious diseases.

Keywords: Zika virus, Animal model, Mice, Pathology, Neuroinflammation, TSPO, DPA-714, PET imaging, Therapeutics

Introduction:

ZIKV is a human pathogenic arthropod-borne flavivirus that is closely related to dengue, West Nile, Japanese encephalitis and yellow fever viruses [1, 2]. Mortality is not a common feature of human infection with ZIKV, which is generally asymptomatic and self-limiting in most individuals. However, severe disease in adults is characterized by neurological complications including Guillain-Barré syndrome (GBS) [3, 4] or in a few cases, encephalopathy [5], meningoencephalitis [6], and acute myelitis [7]. ZIKV infection in pregnant women is a major global public health concern because of its linkage to congenital abnormalities including microcephaly, spontaneous abortion, and intrauterine growth restriction [8]. Many questions remain unanswered about the mechanisms by which ZIKV might cause severe neurological sequelae including congenital defects. As ZIKV continues to spread, so does concern about the association of ZIKV infection and the development of severe clinical complications.

In vivo molecular imaging has been used to characterize disease progression and evaluate drugs in the areas of neuroscience, cardiovascular, inflammation and oncology, but the application of imaging to infectious diseases has been limited (reviewed in [9]). More specifically, application of *in vivo* imaging in evaluation of animal models of ZIKV

infection has not been described. The power of molecular imaging lies in its ability to provide a noninvasive, spatiotemporal measurement of pathogen infection and its effects on key biological processes such as metabolism and inflammation. Numerous molecular imaging probes are available to characterize the host response to virus infection. Positron emission tomography (PET) imaging using 2-deoxy-2-[^{18}F]fluoro-D-glucose ([^{18}F]FDG) has been commonly used as a radiotracer in clinical and basic research. [^{18}F]FDG is an analog of glucose that accumulates preferentially in cells based on their metabolic activity rather than their cell type, and has been used to assess tissue metabolism. In general, [^{18}F]FDG has been used substantially to assess inflammation. As key components of the inflammatory response, infiltrating inflammatory cells utilize glucose at a much higher rate than peripheral non-inflammatory cells [10]. Therefore, the increased glucose metabolism of these inflammatory cells has become an important and frequently used target in PET imaging of inflammation. [^{18}F]FDG uptake, however, is not cell-type specific, making it sometimes difficult to differentiate signal derived from an active inflammatory response from signal originating from hypermetabolic cells or tissues *not* associated with the local inflammatory response (e.g. brain or muscle). In contrast, the radiotracer [^{18}F]DPA-714 monitors the surface molecule TSPO [11] which is highly upregulated in central nervous system (CNS) activated microglia, macrophages, neutrophils, lymphocytes, and reactive astrocytes [12-19], and has therefore emerged as a promising target for the dynamic analysis of neuroinflammation using PET imaging.

Immunocompetent adult mice infected with ZIKV can develop a transient viremia, but do not demonstrate signs of morbidity or mortality. In contrast, knockout mice deficient in the type I or type II interferon (IFN) response were found to be highly

susceptible to ZIKV infection where virus replicated in multiple organs including the brain [20-23]. To assess neuroinflammation associated with ZIKV infection, [^{18}F]DPA-714 PET imaging was performed in a recently described murine model of ZIKV infection where the type I IFN response is transiently suppressed. This model utilizes wild-type C57BL/6 mice treated with a non-cell depleting monoclonal antibody (MAb-5A3) to disrupt type I IFN signaling [24]. Mice infected by intraperitoneal inoculation were highly susceptible incurring 100% mortality where the animals experienced weight loss, viremia, hind-limb paralysis and severe neuropathology. The most significant histopathological findings occurred in the CNS where lesions represent an acute to subacute encephalitis/encephalomyelitis that is characterized by neuronal death, astrogliosis, microgliosis, scattered necrotic cellular debris, and inflammatory cell infiltrates [24]. This model of ZIKV pathogenesis is valuable for evaluating medical countermeasures and the pathogenic mechanisms of ZIKV because it allows immune responses to be elicited in immunologically competent mice with IFN I blockade induced at the time of infection.

In the current study, ZIKV-infected mice administered MAb-5A3 (5A3) antibodies to disrupt IFN signaling were evaluated at early, middle, and late stages of infection by PET imaging using [^{18}F]DPA-714. To control for effects on neuroinflammation stemming from 5A3 activity or ZIKV alone, 5-week-old female C57BL/6 mice were separated into three treatment groups: 1) PBS+5A3, 2) ZIKV+PBS, and 3) ZIKV+5A3. Individual cohorts of mice from each group were evaluated for changes in neuroinflammation at days 3, 6, and 10 post-infection (PI). Histologic analysis of tissue specimens was performed to correlate the imaging findings with the

classical means of assessing the neuropathology owing to ZIKV infection. Unlike a histologic assessment, imaging approaches have the potential to dynamically characterize in a live animal model of ZIKV infection the disease process in a functional context. This approach can be applied across a broad spectrum of viruses and can be used to evaluate drug therapy both preclinically and clinically.

Materials and Methods:

Virus

ZIKV strain DAK AR D 41525 isolated in 1984 from *Aedes africanus* mosquitoes in Senegal was obtained from the World Reference Center for Emerging Viruses and Arboviruses (R. Tesh, University of Texas Medical Branch) where it was initially amplified, passaged once each in AP61 and C6/36 cells, and twice in Vero cells. Subsequently, for infection studies in this report, the virus was passaged again in Vero cells (ATCC, CCL-81) and fidelity was verified by sequence analysis [25].

Mouse Infection Studies

Female C57BL/6 mice (n = 15/group; Jackson Laboratories) five weeks of age were injected IP with a total of 3.0 mg in three doses (2.0 mg first dose, 0.5 mg sustaining doses) of 5A3 (produced by Leinco Technologies, St. Louis, MO) [26, 27] or phosphate buffered saline (PBS) on day -1, day +1, and day +4 PI. A prior study characterizing this antibody indicated that a large bolus is needed to saturate the IFNAR-1 receptor pool and the half-life of a 2.0 mg injected dose is 5.2 days [26]. On day 0, mice were infected with 6.4 $\log_{10}$ PFU of ZIKV strain DAK AR D 41525 by IP exposure route in a total volume

of 200 µL. The mean time-to-death (MTD) for this mouse model of ZIKV infection is reported to be 9.7 days [24].

This work was supported by an approved U.S. Army Medical Research Institute of Infectious Diseases (USAMRIID) IACUC animal research protocol. Research was conducted under an IACUC approved protocol in compliance with the Animal Welfare Act, PHS Policy, and other Federal statutes and regulations relating to animals and experiments involving animals. The facility where this research was conducted is accredited by the Association for Assessment and Accreditation of Laboratory Animal Care, International and adheres to principles stated in the Guide for the Care and Use of Laboratory Animals, National Research Council, 2011.

qRT-PCR Assay to Determine Viral Titer in Sera and Brain

Mouse serum samples were inactivated using a 3:1 ratio of TRIzol LS Reagent (Thermo Fisher Scientific, Waltham, MA). Tissues were homogenized in 1X Minimum Essential Medium with Earle's Salts and L-glutamine (MEM) with 1% penicillin/streptomycin and 5% heat-inactivated fetal bovine serum (FBS-HI) using a gentleMACS dissociator (Miltenyi Biotec, San Diego, CA) followed by centrifugation at 10,000 x g for 10 minutes and the supernatant was stored at -80°C until further evaluation. Supernatant was inactivated using a 3:1 ratio of TRIzol LS. Total nucleic acid from all samples was purified using the EZ1 Virus Mini Kit v 2.0 (Qiagen, Valencia, CA) and the EZ1 Advanced XL robot (Qiagen) according to the manufacturer's recommendations. Samples were eluted in 60µL. Viral load was determined using a real-time RT-PCR assay specific to the 5'-untranslated region of ZIKV. Specific amplification detection was accomplished using a forward primer (5'-

GARTCAGACTGCGACAGTTCGA), reverse primer (5'-CCAAATCCAAATTAAACCTGTTGA), and probe (5'-ACTGTTGTTAGCTCTCGC–MGBNFQ). A standard curve was generated using serial dilutions of the challenge virus having PFU/mL titers determined by plaque assay. Five µL of extracted nucleic acid were run in triplicate on the LightCycler 480 (Roche Diagnostics, Inc., Indianapolis, IN) using SuperScript One-Step RT-PCR (Thermo Fisher Scientific), and samples were considered negative if the cycle of quantification (Cq) was greater than 40 cycles. This Cq cutoff value was selected because when Cq's are greater than 40 cycles, you are outside of the linear dynamic range of real-time PCR, and thus, can negatively impact data reproducibility. The virus titers were calculated using the standard curve and the LightCycler 480 software, and the final PFU equivalents/mL (PFUe/mL) calculations were determined based on the sample input volumes and the upfront sample dilutions.

Virus Titration

Vero cells were plated at $3x10^5$ cells/well in a six-well plate and incubated overnight at 37°C, 5% CO_2. Serial dilutions of samples were made in 1X MEM with 1% penicillin/streptomycin and 5% heat-inactivated FBS. Uninfected-control and serially diluted samples were incubated with the Vero cells for one hour at 37°C, 5% CO_2 for virus adsorption. The inoculum was removed and a 1:1 mixture of 0.8% (w/v) Seaplaque agarose and 2X Basal Medium Eagle with Earle's Salts (EBME) solution containing 2X EBME, 10% FBS-HI, 2% penicillin/streptomycin, 50 µg/mL gentamicin, and 2.5 µg/mL Fungizone/Amphotericin B was added. After addition, the 0.4% Seaplaque agarose/2X EBME overlay was incubated at room temperature for 30 minutes to allow the overlay to solidify. Vero cells were incubated with the overlay at 37°C, 5% CO_2 for five days

before the overlay was removed. Cells were fixed and plaques were visualized by a 20 minute addition of 10% formalin with 50% Crystal Violet solution followed by a wash with water.

PET Radiotracer

[^{18}F]DPA-714 was obtained from the Imaging Probe Development Center, NIH, Rockville, MD and was produced by employing slight modifications to procedures already reported [28], and using a commercially available GE TRACERLab FX-N Pro synthesizer [29]. Ready-to-inject, >99 % radiochemically pure [^{18}F]DPA-714 (formulated in physiological saline containing ~10 % ethanol) was obtained with 30-40% (n = 12) non-decay-corrected yields and the specific activity at the end of the 70-minute radiosynthesis ranged from 48 to 200 GBq/μmol.

PET/CT Imaging and Data Acquisition

On days 3, 6, and 10 post-infection, mice (n=5/group/day) were bled for determination of viremia by qRT-PCR and then PET/CT scanned. PET/CT scanning was performed using an Inveon preclinical PET/CT system (Siemens Medical Solutions, Knoxville, TN) with a spatial resolution of ~1.5 mm full width at half maximum at the center of the field of view. Mice were anesthetized with isoflurane (4% induction, 2% maintenance) delivered in oxygen. Once anesthetized, animals were administered ~8.0 MBq of [^{18}F]DPA-714 in ~150 μL volume via IV tail vein injection and were allowed to wake in their home cages for a 60-minute radiotracer uptake phase. Just prior to scanning, mice were reanesthetized with isoflurane and placed in the scanner positioned in the center of the PET field of view. A single, 15-minute static PET scan was initiated followed immediately by CT scanning (80 kV, 500 μA, 98 μm, 360º rotation in 220

steps). During all imaging procedures, animal respiration rate and body temperature were monitored and maintained using an M2M-BioVet™ small animal physiological monitoring system (M2M imaging, Cleveland, OH). When scanning was completed, mice were euthanized via CO_2 asphyxiation and brains were removed and preserved for infrared (IR), immunohistological and tissue viral titer analysis. PET and CT imaging data were reconstructed and [^{18}F]DPA-714 biodistribution was quantified and evaluated for differences between treatment groups at days 3, 6, and 10 post-treatment and compared to historic PBS-administered controls.

Image Reconstruction and Data Analysis

All image reconstructions were performed using Siemens' Inveon Acquisition Workplace v2.0 software package (Siemens Medical Solutions, Knoxville, TN). Hounsfield Unit (HU) calibrated CT data were reconstructed using a Feldkamp reconstruction algorithm with a Shepp-Logan reconstruction filter, slight noise reduction, and beam hardening correction applied. Decay-corrected PET images were reconstructed using an iterative OSEM3D/MAP algorithm with scatter, dead time, and CT-based attenuation correction. The reconstruction parameters were 18 subsets, 3 iterations in a 128 x 128 matrix with a target resolution of 1.2 mm. PET images were coregistered to corresponding CT data using VivoQuant v2.5 image processing software (inviCRO, LLC, Boston, MA) and were subsequently coregistered to a 3D mouse brain atlas (included in VivoQuant software package) so that brain [^{18}F]DPA-714 biodistribution could be quantified. PET imaging data were reported in terms of percent injected dose per gram of tissue (%ID/g), calculated as a ratio of tissue radioactivity concentration (Bq/g) at time of scan to total injected activity (Bq) at time of scan.

Histology

A necropsy was completed and brains were collected and immersion-fixed in 10% neutral buffered formalin for at least 2 days. Brains were subsequently trimmed and processed according to standard protocols [30]. Histology sections were cut at 5 to 6 µM on a rotary microtome, mounted onto glass slides, and stained with hematoxylin and eosin (HE). Unblinded histological examination was performed by a board-certified veterinary pathologist.

ZIKV RNA In situ Hybridization (ISH)

In situ hybridization was performed using RNAscope® 2.5 HD RED kit according to the manufacturer's recommendations (Advanced Cell Diagnostics, Hayward, CA). Briefly, 20 ZZ probes set targeting the 1550-2456 fragment of the ZIKV polyprotein gene with Gene bank accession KJ776791.1 were synthesized. After deparaffinization and peroxidase blocking, the sections were heated in antigen retrieval buffer and then were digested by proteinase. The sections were covered with ISH probes and incubated at 40°C in a hybridization oven for two hours. They were rinsed and the ISH signal was amplified by applying Pre-amplifier and Amplifier conjugated with HRP. A red substrate-chromogen solution was applied for 10 minutes at room temperature. The slides were further stained with hematoxylin, air dried, and mounted.

Infrared (IR) and Immunofluorescent Imaging

Formalin-fixed, paraffin-embedded mouse brain sections on slides were deparaffinized in xylene and rehydrated through graded ethanol (100%, 95%, 90%, and 70%). Antigen was retrieved by citric acid-based antigen unmasking solution (Vector Laboratories) during 10 minutes at 95-100^{o}C. After three washes with PBS (pH 7.4), the

sections were blocked with 10% normal donkey serum in PBS-tween (0.1%; PBS-T) for one hour at room temperature. The sections were incubated with primary antibody, goat anti-Iba-1 (3 µl/mL; Novus Biotechnology), diluted in 10% normal donkey serum in PBS-T overnight at 4°C. After washing in PBS-T (3x5 min), the sections were incubated overnight at 4°C with secondary antibodies diluted in 10% normal donkey serum in PBS-T. For standard immunofluorescence, the secondary antibodies were donkey anti-goat Alexa Fluor 594 (1:400; Invitrogen; pseudocolored green). The nuclei were stained with Hoecht's. For IR analysis, the secondary antibody was donkey anti-goat IRDye 680RD (1:1500; LI-COR Biosciences). The sections were subsequently washed in PBS-T (3x10 min), PBS (3x5 min), and water (2x5 minutes). For immunofluorescence, the sections were cover slipped with Fluoromount-G (SouthernBiotechnology). Images were captured on a Zeiss LSM 700 confocal system and processed with Zen 2011 software. Sections for IR analysis were air-dried overnight. A LI-COR-Odyssey CLx (LI-COR Biosciences) scanned sections at 42 µm/pixel resolution. The average intensity of Iba-1 on each slide was obtained from fields-of-interest drawn around each section with the LI-COR-Odyssey analysis software and two slides per brain were scanned. Negative control staining, for which the primary antibodies were omitted, showed no detectable labeling in immunofluorescence or IR imaging.

Statistical Analysis

Statistical analysis was carried out using SAS/STAT® software, version 9.4 (SAS Institute Inc.). All values are means ± SD, with a testing level (α) of 0.05 and adjusted P values as indicated. $P<0.05$ signifies statistical significance. One-way ANOVA with post-hoc Dunnett's one-tailed *t* tests were used to compare each treatment group by day

with historical control data. One-way ANOVA with post-hoc Tukey-Kramer tests were used to compare between treatment groups by day.

Results:

Viral Titers in Sera and Brains of ZIKV-Infected Mice

Prior to PET scanning at days 3, 6 and 10 post-infection, mice designated for imaging from each treatment group were bled and viral titers in sera were determined by qRT-PCR (Figure 1a). For the PBS+5A3 and ZIKV+PBS treatment groups, no viremia was detected in any mouse at any time point tested. In the group susceptible to ZIKV infection (ZIKV+5A3), average viremia was highest (~5.5 $\log_{10}$ PFUe/mL; n=5) at day 3 PI and decreased at both days 6 (~4.2 $\log_{10}$ PFUe/mL; n=5) and 10 PI (~3.0 $\log_{10}$ PFUe/mL; n=4). These data demonstrate a productive infection in the subjects challenged with ZIKV and treated with 5A3 with the exception of one mouse at day 10 PI.

At the conclusion of each PET scan, mice were euthanized and brains were harvested for viral titer determination (Figure 1b). As expected, the mice in the PBS+5A3 treatment group showed no detectable viral titers in brain at days 3, 6 or 10 post-infection. In the ZIKV+PBS treatment group, four out of the five mice tested at each time point also showed no detectable viral titers in brain, however, a single mouse at each time point tested (days 3, 6, and 10 post-infection) had viral brain titers of ~3.9, ~6.8, and ~4.9 $\log_{10}$ PFUe/g, respectively, suggesting perhaps some level of viral CNS penetration and subsequent clearance with no detectable viremia. In contrast to the decreasing viremia that was measured in the susceptible ZIKV+5A3 animals, brain titers

in this group were shown to increase over time as determined by qRT-PCR from brain homogenates. From day 3 PI to day 10 PI, brain viral titers increased from an average of ~5.3 $\log_{10}$ PFUe/g at day 3 PI to an average of ~6.95 $\log_{10}$ PFUe/g in the remaining living mice (n=4/5) by day 10 PI. It should be noted, however, that at days 3 and 10 post-infection, a single mouse at each time point, respectively, had brain viral titers below the limit of detection for our assay. To confirm the presence of infectious virus in the brain, qRT-PCR titers were verified by conventional plaque assay. Altogether, these data are consistent with our previous findings [24] and those of others [20-23], and demonstrate a substantial increase in ZIKA neuroinvasion when IFN-I signaling is blocked.

[^{18}F]DPA-714 Uptake in Brains of ZIKV-Infected Mice

To evaluate the ability of *in vivo* PET imaging to detect ZIKV-induced neuroinflammation in mouse brain, we used [^{18}F]DPA-714, a PET radiotracer that is specific for TSPO [11], a biochemical marker of neuroinflammation that is highly upregulated in activated microglia, CNS macrophages and reactive astrocytes [12-19]. By as early as day 3 PI, ZIKV-infected mice treated with MAb-5A3 showed a modest but significant (approximately 2-fold) increase in mean whole-brain [^{18}F]DPA-714 binding (2.21±0.14 %ID/g; n=5) compared to historic PBS controls (Fig. 2a and b). By days 6 and 10 post-infection, the increase in mean whole-brain [^{18}F]DPA-714 binding in ZIKV+5A3 mice was approximately 4 (4.48±1.35 %ID/g; n=5) and 6-fold (5.70±3.19 %ID/g; n=3), respectively, compared to historic PBS controls. Based on brain subregion analysis, all brain regions evaluated (olfactory bulb, striatum, pallidum, hippocampus, thalamus, hypothalamus, cortex, corpus callosum, white matter, cerebellum, pons, and medulla) were increased similar to the whole brain. Of note, one of the three mice from

the ZIKV+5A3 group at day 10 PI had [^{18}F]DPA-714 binding (2.25 %ID/g) similar to the ZIKV+PBS (2.53±0.41 %ID/g, n=5) and PBS+5A3 (1.97±0.37 %ID/g, n=5) control groups at day 10 PI, which reduced the mean whole-brain [^{18}F]DPA-714 binding for this group. Moreover, viral RNA was not detected in the brain of this mouse at day 10 PI (Figure 1b). This subject was not excluded from our analyses because viremia was not assessed in this subject at day 3 and/or day 6 PI allowing for the possibility that this subject was infected and cleared the virus prior to CNS penetration, i.e. it recovered from the neuroinflammatory disease prior to day 10 or it never became infected.

ZIKV alone (ZIKV+PBS) showed a similar modest (2.25±0.11 %ID/g; n=5) but significant increase in mean whole-brain [^{18}F]DPA-714 binding at day 3 PI relative to historic PBS controls. However, in contrast to ZIKV-infected mice with impaired IFN signaling (ZIKV+5A3), mean whole-brain [^{18}F]DPA-714 binding in ZIKV+PBS remained at modest levels at day 6 PI (2.51±0.30 %ID/g, n=5) and returned to the level of historic PBS controls by day 10 PI suggesting that ZIKV infection in the presence of IFN signaling is sufficient to produce a mild yet transient neuroinflammatory effect measureable by [^{18}F]DPA-714 PET imaging. Importantly, 5A3 treatment in the absence of ZIKV had no detectable effect on mean whole-brain [^{18}F]DPA-714 uptake and shared a similar tracer uptake profile as the historic PBS control mice at all three time points tested. These results demonstrate for the first time the ability of [^{18}F]DPA-714 PET imaging to detect and quantify ZIKV-related neuroinflammation disseminated throughout the brains of infected mice.

Histopathology Findings

To confirm the *in vivo* findings of ZIKV-induced neuroinflammation as determined by [^{18}F]DPA-714 PET imaging, brain sections from the PET imaged mice were assessed for pathology, ISH to detect viral RNA, and IR and immunofluorescent detection of Iba-1, a microglia/macrophage-specific calcium-binding protein that is highly upregulated during neuroinflammation [31]. Consistent with our imaging results, brains from the susceptible ZIKV+5A3 treatment group exhibited histopathological lesions consistent with encephalitis with minimal microgliosis beginning as early as day 3 PI (Figure 3a). By days 6 and 10 PI, microgliosis was more pronounced, with the presence of mononuclear cell perivascular cuffs peaking at day 6 PI and waning by day 10 PI (Figure 3b, c). Other histological findings consistent with encephalitis include minimal necrotic cellular debris scattered throughout the parenchyma (days 6 and 10 PI), and neuronal degeneration and necrosis observed in the cerebrum as early as day 6 PI and becoming more pronounced and widespread on day 10 PI (cerebrum, hippocampus, and thalamus). Additionally, variable minimal perivascular edema and hemorrhage was present on both days 6 and 10 PI. Moreover, ZIKV RNA was detected by ISH in the cerebral cortex on day 6 and 10 PI, and in the hippocampus on day 10 PI in mice administered ZIKV+5A3 (Figure 3e, f). Mice administered ZIKV+PBS exhibited no signs suggestive of ZIKV infection on days 3 or 6 PI; however, 1/5 animals exhibited minimal lesions consistent with encephalitis (perivascular cuffing, microgliosis) on day 10 PI that may be attributable to ZIKV infection, though no viral RNA was detected in this animal by ISH. As expected, animals administered 5A3+PBS exhibited no CNS

lesions suggestive of ZIKV infection and no viral RNA was detected by ISH at any of the time points tested.

In terms of Iba-1 expression, no statistical difference was observed by IR imaging at days 3 and 6 PI for any of the treatment groups tested, PBS+5A3, ZIKV+PBS, or ZIKV+5A3 (Fig. 4a and b, first two rows). At day 6 PI, however, whole-brain Iba-1 expression in the susceptible ZIKV+5A3 group is modestly, though not significantly, increased. By day 10 PI, and in agreement with the [^{18}F]DPA-714 findings, Iba-1 expression was significantly increased (approximately 4-fold) in the ZIKV+5A3 group compared to either of the control groups (Fig. 4a and b, bottom row). These findings were confirmed by immunofluorescent labeling of Iba-1 in these brains (Fig. 4c and d). Importantly, the single animal in the ZIKV+5A3 treatment group at day 10 post-infection that showed no appreciable Iba-1 labeling by IR imaging was the same animal that at day 10 PI showed no detectable virus in the brain (Fig. 1b) and no significant whole-brain [^{18}F]DPA-714 binding over controls (Fig. 2a and b). These data are consistent with and serve to confirm our *in vivo* PET imaging results. These results also demonstrate the ability of *in vivo* [^{18}F]DPA-714 PET imaging to provide a more sensitive measure of ZIKV-induced neuroinflammation than Iba-1 IR or immunofluorescent imaging.

Discussion:

Here, we demonstrate that [^{18}F]DPA-714 PET imaging is a sensitive method capable of identifying and quantifying ZIKV-induced neuroinflammation in a previously described mouse model of ZIKV neurological disease. In this model, C57BL/6 mice with a transiently suppressed IFN-I response by treatment with MAb-5A3 are highly

susceptible to peripheral ZIKV challenge and [^{18}F]DPA-714 PET imaging was able to detect significant neuroinflammation at day 3 PI compared to uninfected, 5A3 treated mice. Neuroinflammation continues to increase at days 6 and 10 PI in the 5A3-treated, ZIKV-infected mice. In addition, [^{18}F]DPA-714 PET imaging was able to detect modest, yet significant neuroinflammation in immunocompetent mice exposed to ZIKV and treated with PBS at day 3 PI demonstrating the induction of neuroinflammation in the absence of 5A3 treatment. Neuroinflammation in this group begins to wane by day 6 PI, and is indistinguishable from historic PBS controls by day 10 PI. This transient, low-level neuroinflammation, in combination with the lack of viremia and virus in the brain, may result from the innate and adaptive immune responses against ZIKV infection. Taken together, these results indicate that neuroinflammation plays an important role in the pathogenesis of ZIKV infection and that [^{18}F]DPA-714 PET imaging can very sensitively detect neuroinflammation in both immune-compromised and immunocompetent mice exposed to ZIKV.

Previous studies have shown that ZIKV infection in animal models is associated with the activation of immune responses, cellular infiltration, inflammation and neural damage in the CNS [24, 32]. It is interesting to note that in our study, significant neuroinflammation was detected throughout the brains of mice despite limited detection of viral RNA by ISH (Figure 3) and qRT-PCR (Figure 1b). These findings suggest that the host inflammatory response is associated with the ZIKV-induced neuropathogenesis which is not solely caused by virus-mediated damage. This is consistent with a recent study in *Stat2*$^{-/-}$ mice demonstrating that ZIKV pathogenicity associates with the degree of inflammatory immune response in the CNS of infected mice and does not correlate

with viral RNA levels [33]. The immune response plays a critical role in the outcome of alphavirus-induced CNS disease as well. Increasing evidence suggest that fatal alphavirus encephaloymyelitis is mediated by the immune response to virus infection rather than direct virus replication (reviewed in [34, 35]). Collectively, these results suggest that the use of [^{18}F]DPA-714 PET to measure ZIKV-induced neuroinflammation may provide a more accurate quantification of ZIKV pathology than viral titer measurements alone. Therefore, [^{18}F]DPA-714 PET imaging may not only more accurately monitor disease progression during ZIKV infection, but it may also serve as a dynamic measure for assessment of drug efficacy.

The results of the current study are also consistent with previous studies that used AG129 mice which lack interferon α/β and γ receptors (IFN α/β and γ). ZIKV is lethal in AG129 mice, but significant neuropathology is observed prior to death [20-23]. Neurodegeneration, as evidenced by necrotic cellular debris, nuclear fragments, hyper-eosinophilic cytoplasm and pycnotic nuclei is observed in AG129 mice infected with ZIKV. Inflammatory cells such as lymphocytes, monocyte-macrophages, neutrophils and T-cells are also seen in the parenchyma of the brain [20, 21]. In AG129 mice as well as in neonatal C57BL/6 mice infected with ZIKV, genes associated with inflammation and cellular infiltration are significantly upregulated in the brain [22]. The gene expression in AG129 mice was consistent with inflammatory infiltrates, activated microglia and astrocytes, while in neonatal C57BL/6 mice with an intact immune system, a phenotype associated with a significant T cell response was noted [22]. Thus, the results of the current study together with previously published work demonstrate the importance of the IFN signaling pathway in the resolution of ZIKV infection, and that neuroinflammation is

a key component of ZIKV infection that if left unresolved, leads to death (e.g., ZIKV+5A3 group versus ZIKV+PBS).

[^{18}F]DPA-714 PET imaging also proved to be more sensitive for the detection of small changes in neuroinflammation during ZIKV infection relative to classical immunohistochemical methods. [^{18}F]DPA-714 binding was significantly increased at days 3, 6 and 10 PI in 5A3-treated, ZIKV-infected mice compared to uninfected, 5A3-treated mice, while significant Iba-1 staining was only noted at day 10 PI. In addition, [^{18}F]DPA-714 binding was significantly increased at day 3 PI in the ZIKV+PBS treatment group while the change was undetected by Iba-1 staining. These findings demonstrate the ability of PET imaging to detect pathology/neuroinflammation earlier and throughout the course of ZIKV infection with greater sensitivity than classical methods, and that the approach can be used to dynamically study early pathogenic events associated with ZIKV and potentially other neurotropic viral infections. Moreover, it may be possible to define distinct disease stages or mechanisms associated with the pathogenesis of ZIKV infection or other neurotropic viruses. For example, PET imaging could identify routes of neuroinvasion or mechanisms of blood-brain barrier permeability and then quickly assess this route or mechanism in related or different neurotropic viruses, thus allowing this technology to expedite the process of expanding an efficacious therapeutic for one virus, to potentially others.

Conclusions:

Our findings demonstrate that global neuroinflammation plays a significant role in the progression of ZIKV infection and that [^{18}F]DPA-714 PET imaging is a sensitive tool

relative to histology for the detection of neuroinflammation. [^{18}F]DPA-714 PET imaging and potentially other PET probes may be useful in dynamically characterizing the pathology associated with neurotropic viruses and the evaluation of therapeutics being developed for treatment of infectious diseases.

Acknowledgments:

The authors would like to thank Dr. Sarah Norris for her assistance in performing the statistical analysis, Ms. Tara Kenny for the preparation of the ZIKV strain DAK AR D 41525 stocks used in the study. The authors would also like to thank Dr. Christopher Kane, Dr. Sina Bavari and LTC Todd Kijek for their assistance in securing funding for performance of the study. Funding for the performance of the studies was provided by Department of Defense Chemical Biological Defense Program through the Defense Advanced Research Projects Agency (DARPA) under the U.S. Army Medical Research Institute of Infectious Diseases (USAMRIID) project number 15094637. Dr. Bradley S. Hollidge participated in this research while holding an NRC Research Associateship award at USAMRIID. Opinions, interpretations, conclusions, and recommendations stated within the article are those of the authors and are not necessarily endorsed by the U.S. Army.

Conflict of interests:

The authors declare that they have no conflicts of interest.

References:

1. Gatherer D, Kohl A (2016) Zika virus: a previously slow pandemic spreads rapidly through the Americas. J Gen Virol 97(2):269-273
2. Pierson TC, Diamond MS (2013) Flaviviruses. In: Fields Virology, 6th ed. Ed. Knipe DM, Howley PM. Philadelphia, PA: Lippincott Williams & Wilkins, pp 747-794
3. Cao-Lormeau VM, Blake A, Mons S et al (2016) Guillain-Barre Syndrome outbreak associated with Zika virus infection in French Polynesia: a case-control study. Lancet 387(10027):1531-1539
4. Oehler E, Watrin L, Larre P et al (2014) Zika virus infection complicated by Guillain-Barre syndrome--case report, French Polynesia, December 2013. Euro Surveill 19(9)
5. Roze B, Najioullah F, Signate A et al (2016) Zika virus detection in cerebrospinal fluid from two patients with encephalopathy, Martinique, February 2016. Euro Surveill 21(16)
6. Carteaux G, Maquart M, Bedet A et al (2016) Zika Virus Associated with Meningoencephalitis. N Engl J Med 374(16):1595-1596
7. Mecharles S, Herrmann C, Poullain P et al (2016) Acute myelitis due to Zika virus infection. Lancet 387(10026):1481
8. Brasil P, Pereira JP Jr, Moreira ME et al (2016) Zika Virus Infection in Pregnant Women in Rio de Janeiro. N Engl J Med 375(24):2321-2334
9. Bocan TM, Panchal RG, Bavari S (2015) Applications of in vivo imaging in the evaluation of the pathophysiology of viral and bacterial infections and in development of countermeasures to BSL3/4 pathogens. Mol Imaging Biol 17(1):4-17

10. Wu C, Li F, Niu G, Chen X (2013) PET Imaging of Inflammation Biomarkers. Theranostics 3(7):448-466
11. Lavisse S, Guillermier M, Herard AS et al (2012) Reactive astrocytes overexpress TSPO and are detected by TSPO positron emission tomography imaging. J Neurosci 32(32):10809-18
12. Bird JL, Izquierdo-Garcia D, Davies JR et al (2010) Evaluation of translocator protein quantification as a tool for characterising macrophage burden in human carotid atherosclerosis. Atherosclerosis 210(2):388-391
13. Gaemperli O, Shalhoub J, Owen DR et al (2012) Imaging intraplaque inflammation in carotid atherosclerosis with 11C-PK11195 positron emission tomography/computed tomography. Eur Heart J 33(15):1902-1910
14. Hatori A, Yui J, Yamasaki T et al (2012) PET imaging of lung inflammation with [^{18}F]FEDAC, a radioligand for translocator protein (18 kDa). PloS One 7(9):e45065
15. Hannestad J, Gallezot JD, Schafbauer T et al (2012) Endotoxin-induced systemic inflammation activates microglia: [^{11}C]PBR28 positron emission tomography in nonhuman primates. Neuroimage 63(1):232-239
16. Roeda D, Kuhnast B, Damont A, Dollé F (2012) Synthesis of fluorine-18-labelled TSPO ligands for imaging neuroinflammation with Positron Emission Tomography. J Fluor Chem 134:107-14
17. Ching AS, Kuhnast B, Damont A, Roeda D, Tavitian B, Dollé F (2012) Current paradigm of the 18-kDa translocator protein (TSPO) as a molecular target for PET imaging in neuroinflammation and neurodegenerative diseases. Insights Imaging 3(1):111-119

18. Oh U, Fujita M, Ikonomidou VN et al (2011) Translocator protein PET imaging for glial activation in multiple sclerosis. J Neuroimmune Pharmacol 6(3):354-361
19. Papadopoulos V, Lecanu L (2009) Translocator protein (18 kDa) TSPO: an emerging therapeutic target in neurotrauma. Exp Neurol 219(1):53-57
20. Aliota MT, Caine EA, Walker EC, Larkin KE, Camacho E, Osorio JE (2016) Characterization of Lethal Zika Virus Infection in AG129 Mice. PLoS Negl Trop Dis 10(4):e0004682
21. Dowall SD, Graham VA, Rayner E et al (2016) A Susceptible Mouse Model for Zika Virus Infection. PLoS Negl Trop Dis 10(5):e0004658
22. Lazear HM, Govero J, Smith AM et al (2016) A Mouse Model of Zika Virus Pathogenesis. Cell Host Microbe 19(5):720-730
23. Rossi SL, Tesh RB, Azar SR et al (2016) Characterization of a Novel Murine Model to Study Zika Virus. Am J Trop Med Hyg 94(6):1362-1369
24. Smith DR, Hollidge B, Daye S et al (2017) Neuropathogenesis of Zika Virus in a Highly Susceptible Immunocompetent Mouse Model after Antibody Blockade of Type I Interferon. PLoS Negl Trop Dis 11(1):e0005296
25. Ladner JT, Wiley MR, Prieto K et al (2016) Complete Genome Sequences of Five Zika Virus Isolates. Genome Announc 4(3)
26. Sheehan KC, Lai KS, Dunn GP et al (2006) Blocking monoclonal antibodies specific for mouse IFN-alpha/beta receptor subunit 1 (IFNAR-1) from mice immunized by in vivo hydrodynamic transfection. J Interferon Cytokine Res 26(11):804-819

27. Sheehan KC, Lazear HM, Diamond MS, Schreiber RD (2015) Selective Blockade of Interferon-alpha and -beta Reveals Their Non-Redundant Functions in a Mouse Model of West Nile Virus Infection. PLoS One 10(5):e0128636
28. Damont A, Hinnen F, Kuhnast B et al (2008) Radiosynthesis of [^{18}F]DPA-714, a selective radioligand for imaging the translocator protein (18 kDa) with PET. J Label Compd Radiopharm 51:286–292
29. Kuhnast B, Damont A, Hinnen F et al (2012) [^{18}F]DPA-714, [^{18}F]PBR111 and [^{18}F]FEDAA1106-selective radioligands for imaging TSPO 18 kDa with PET: automated radiosynthesis on a TRACERLAb FX-FN synthesizer and quality controls. Appl Radiat Isot 70:489–497
30. Prophet EB, Mills B, Arrington JB, Sobin LH (1992) Laboratory Methods in Histotechnology. Available from: American Registry of Pathology, Armed Forces Institute of Pathology, Washington, DC USA
31. Ito D, Imai Y, Ohsawa K, Nakajima K, Fukuuchi Y, Kohsaka S (1998) Microglia-specific localisation of a novel calcium binding protein, Iba1. Brain Res Mol Brain Res 57(1):1-9
32. Manangeeswaran M, Ireland DD, Verthelyi D (2016) Zika (PRVABC59) Infection Is Associated with T cell Infiltration and Neurodegeneration in CNS of Immunocompetent Neonatal C57Bl/6 Mice. PLoS Pathog 12(11):e1006004
33. Tripathi S, Balasubramaniam VR, Brown JA et al (2017) A novel Zika virus mouse model reveals strain specific differences in virus pathogenesis and host inflammatory immune responses. PLoS Pathog 13(3):e1006258

34. Griffin DE (2016) Alphavirus Encephalomyelitis: Mechanisms and Approaches to Prevention of Neuronal Damage. Neurotherapeutics 13(3):455-460

35. Steele KE, Twenhafel NA (2010) REVIEW PAPER: pathology of animal models of alphavirus encephalitis. Vet Pathol 47(5):790-805

Figure Legends:

Figure 1. Wild-type mice treated with an IFNAR1-blocking MAb are susceptible to ZIKV. Five-week-old female wild-type C57BL/6 mice were treated with an IFNAR1-blocking MAb (5A3) or PBS by intraperitoneal (IP) injection and exposed to 6 $\log_{10}$ of ZIKV strain DAK AR D 41525 or PBS by IP injection. (**a**) Prior to PET imaging at days 3, 6, and 10 post-infection (PI), ZIKV RNA in serum was determined by qRT-PCR. Data are shown as PFU equivalents (PFUe) per milliliter (mL) after normalization to a standard curve. (**b**) When PET scanning was completed, mice were euthanized and brains were collected, weighed, homogenized, and analyzed by qRT-PCR. Data are shown as PFUe per gram (g) after normalization to a standard curve. (**a** and **b**) Symbols represent individual mice, the line represents the group mean, and the error bars represent the standard deviation. The dotted line represents the assay limit of detection.

Figure 2. *In vivo* PET imaging can detect ZIKV-related neuroinflammation as early as day 3 post-infection (PI). Five-week-old female wild-type C57BL/6 mice were separated into three treatment groups, PBS+5A3, ZIKV+PBS, and ZIKV+5A3, and were IV injected with [^{18}F]DPA-714 at 3, 6, and 10 days PI to quantitatively assess brain neuroinflammation in terms of % injected dose/g tissue (%ID/g). (**a**) Representative

PET/CT mouse brain images (sagittal, coronal and transverse, from left to right) for each treatment group at days 3, 6 and 10 PI. Representative historic PBS control mouse brain images at bottom right. (**b**) Symbols represent the individual mice, the line represents the group mean, and the error bars represent the standard deviation. The dotted line represents the mean species-specific historic measured [^{18}F]DPA-714 binding value in brain for PBS treated mice (~1.06 ± 0.21 %ID/g). *p<0.05, **p<0.01, ***p<0.005, ****p<0.001, one-way analysis of variance (ANOVA).

Figure 3. Microgliosis and ZIKV RNA in ZIKV-infected, wild-type mouse brains treated with MAb-5A3. (**a**-**c**) Brain sections were examined by hematoxylin and eosin, which showed minimal microgliosis at day 3 PI (**a**, arrows), minimal-to-mild microgliosis at day 6 PI (**b**, arrows), and moderate microgliosis at day 10 PI (**c**, circle). Scale bar represents 100 μm. (**d**-**f**) Representative images of ISH staining of ZIKV RNA in the brains of MAb-5A3-treated, ZIKV-infected mice. ZIKV RNA is not present at day 3 PI (**d**), but is present mainly in the cerebral cortex at day 6 PI (**e**). At day 10 PI, ZIKV RNA is present in the hippocampus (**f**) and cerebral cortex. Scale bar represent 50 μm.

Figure 4. Iba-1 is increased in the brains of ZIKV-infected wild-type mice treated with an IFNAR1-blocking MAb. At the conclusion of each PET scan (days 3, 6, and 10 PI), brain sections were imaged and analyzed for Iba-1 expression by infrared (IR) and immunofluorescent imaging for all three treatment groups, PBS+5A3, ZIKV+PBS, and ZIKV+5A3. (**a**) By day 10 PI, the average IR intensity, expressed as fold increase relative to PBS+5A3, was ~4-fold greater than PBS control groups (**p<0.01, one-way

analysis of variance (ANOVA)). Symbols represent the individual mice, the line represents the group mean, and the error bars represent the standard deviation. (**b**) Representative images show increased Iba-1 IR signal in brain sections from ZIKV+5A3 mice compared to PBS control groups. (**c**) Representative CA1 hippocampal and (**d**) cortical sections showing immunofluorescent labeling of Iba-1 (green) and nuclei (blue) in PET imaging mice. Scale bar represents 200 μm.

Figure 1

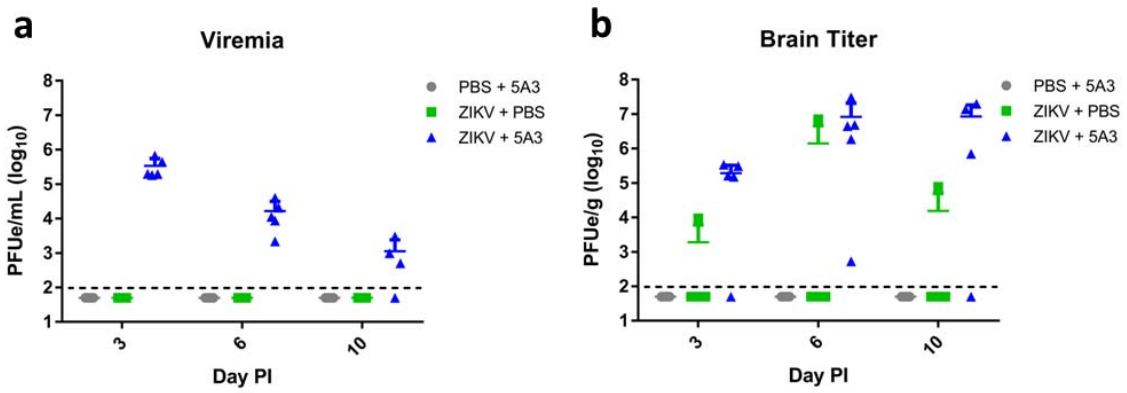
a
Viremia
PFUe/mL (log10)
8
7
6
5
4
3
2
1
3
6
10
Day PI
PBS + 5A3
ZIKV + PBS
ZIKV + 5A3
b
Brain Titer
PFUe/g (log10)
8
7
6
5
4
3
2
1
3
6
10
Day PI
PBS + 5A3
ZIKV + PBS
ZIKV + 5A3

Figure 2

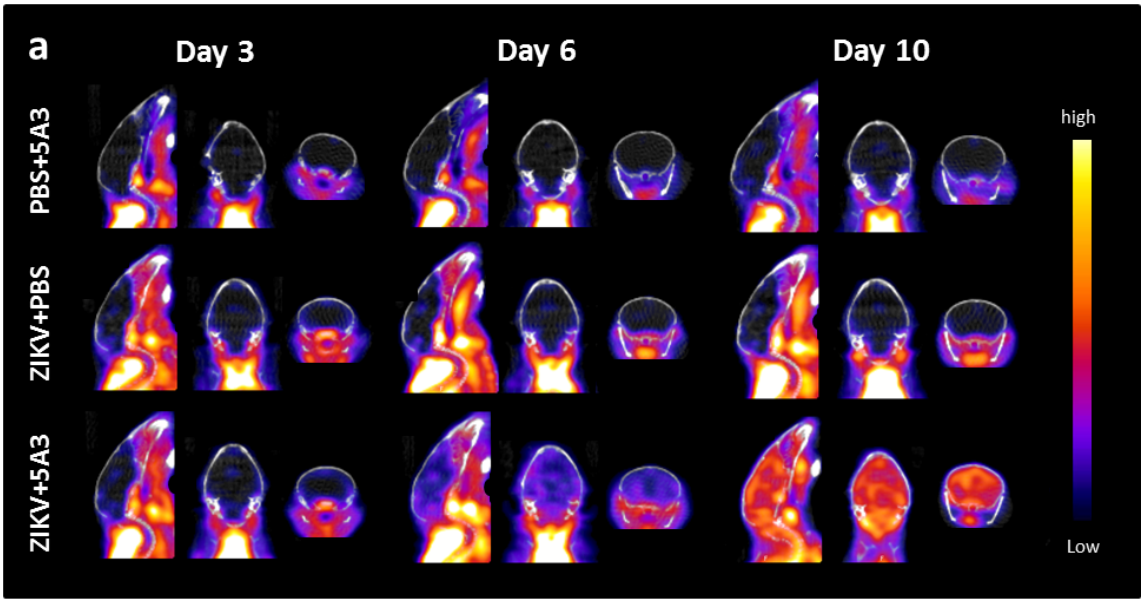

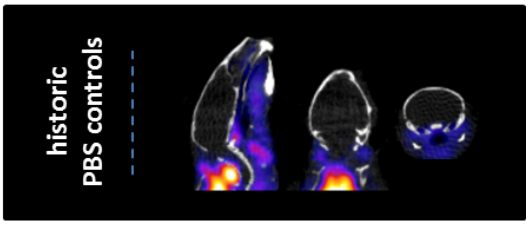

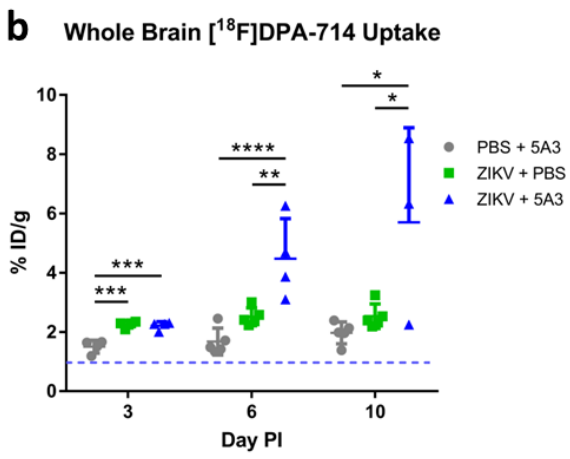

Significance vs. historic PBS controls (1.06 ± 0.21 %ID/g) - - -

treatment group	Day 3 PI (%ID/g)	Day 6 PI (%ID/g)	Day 10 PI (%ID/g)
PBS + 5A3	1.50 ± 0.30	1.67 ± 0.45	1.97 ± 0.37
ZIKV + PBS	2.25 ± 0.11****	2.51 ± 0.30**	2.53 ± 0.41
ZIKV + 5A3	2.21 ± 0.14****	4.48 ± 1.35****	5.70 ± 3.19****

Figure 3

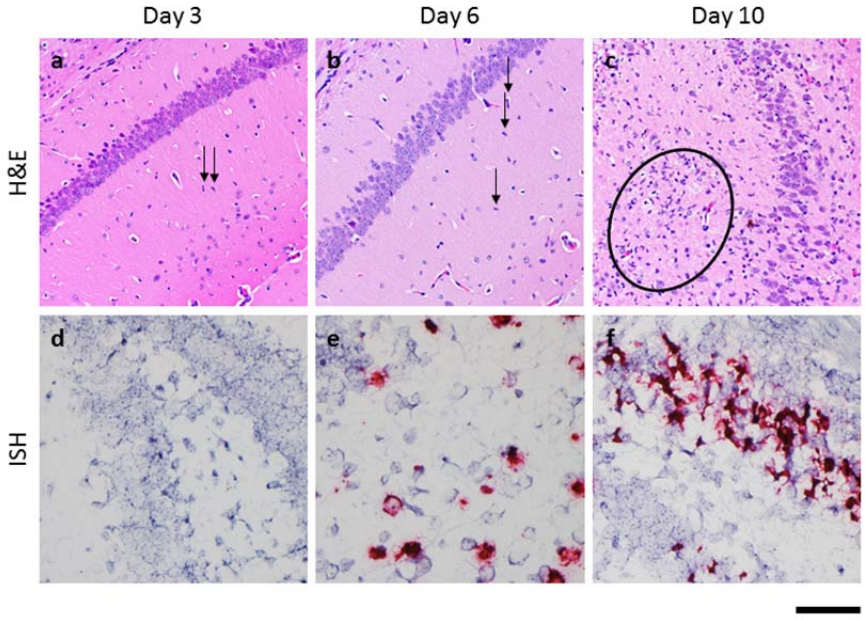

Figure 4

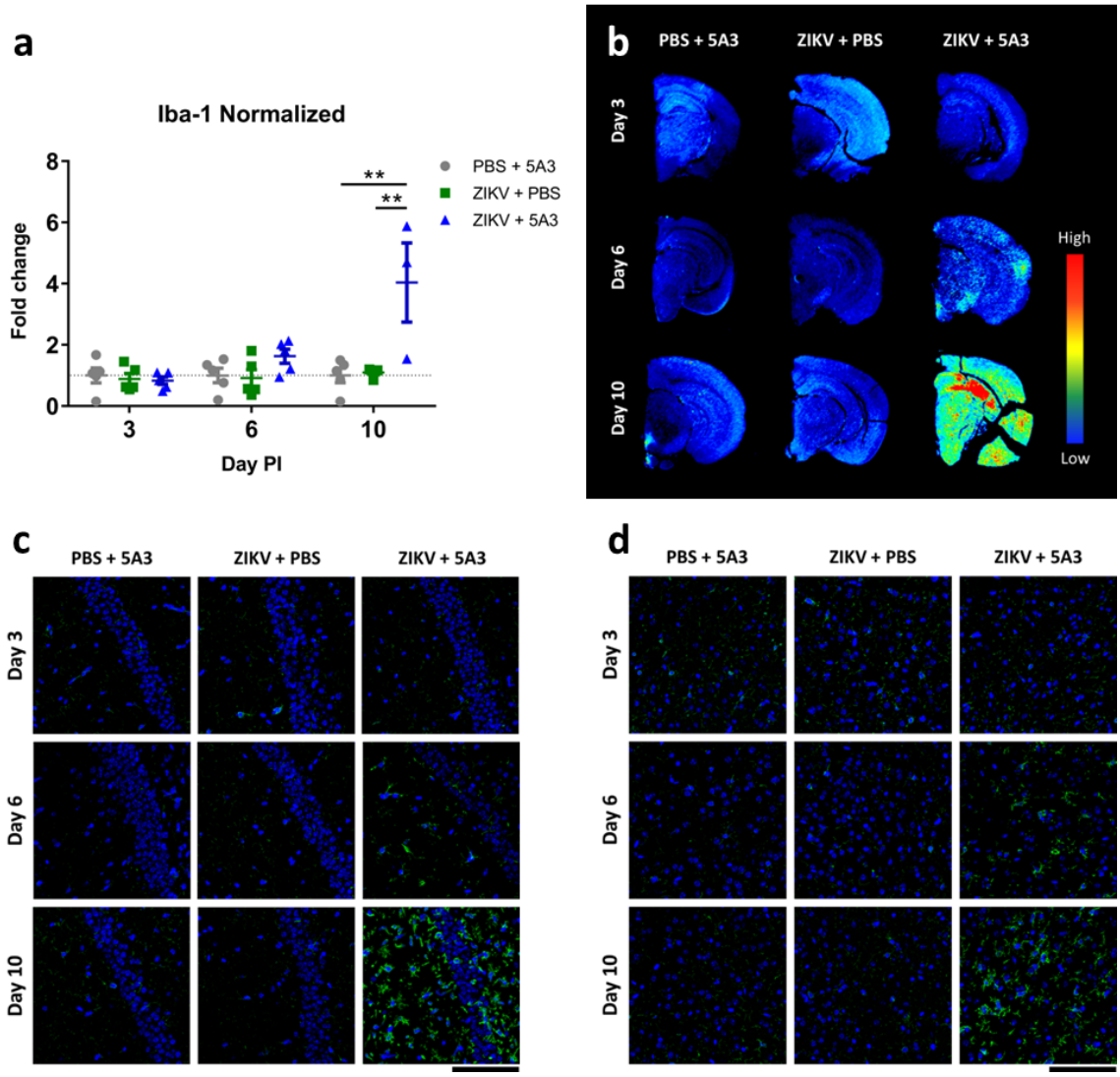
a
Iba-1 Normalized
Fold change
Day PI
PBS + 5A3
ZIKV + PBS
ZIKV + 5A3
**
**
b
PBS + 5A3
ZIKV + PBS
ZIKV + 5A3
Day 3
Day 6
Day 10
High
Low
c
d